Model-Based Wind Estimation using H_∞ Filtering with Flight Test Results

Kenneth C. Gahan*, Jeremy W. Hopwood†, and Craig A. Woolsey‡
Virginia Polytechnic Institute and State University, Blacksburg, VA 24061

I. Introduction

Wind estimation from air vehicle motion is useful for many reasons, including weather forecasting and air traffic management [1, 2]. The ability to estimate wind indirectly (i.e., without specialized instrumentation) is of particular interest due to the increasing ubiquity of small unmanned aircraft systems (UASs) [3] and the unobtrusive/low-cost nature of using operational sensors (e.g., air vehicle GPS, accelerometers, and gyroscopes). A common goal is to extract a slowly varying mean component of the wind from higher frequency fluctuations (gusts or atmospheric turbulence). These bulk flows are used in high fidelity numerical weather models [4] and urban air mobility (UAM) path planning algorithms [5], among several other applications.

Generally, wind estimation methods can be grouped into two major categories: model-based and model-free. Model-based estimation requires accurate aerodynamic and propulsion (aero-propulsive) models of the aircraft to generate state and wind estimates [6, 7]. Model-based methods do not require direct measurement of the wind, such as with an air data sensor, and are thus readily applied to small UASs which typically do not have pitot-static systems. Model-free methods, alternatively, do not require aero-propulsive models but instead use direct air measurements and inertial velocity to resolve wind speed and direction. However, even if a UAS has some form of direct air data measurement, model-free methods may require persistent excitation (i.e., constant maneuvering) to generate accurate wind estimates [8]. This requirement is impractical for normal operations which have significant periods of straight-and-level cruise. For the above reasons, this work focuses on model-based wind estimation.

In many UAS-based wind estimation applications, as surveyed in [9] and [8], some variation of the well-known Kalman filter is used as a state estimator to determine the wind velocity. Examples are a two-stage Kalman filter in [10], an unscented Kalman filter in [11], and the traditional linear Kalman filter in [12]. Such filters are almost always implemented in discrete time, to be compatible with modern sampled data systems for measurement and control, but the continuous-time version of the Kalman filter, known as the Kalman-Bucy filter, is used for comparison in this work.

The Kalman-Bucy filter is the minimum covariance linear state estimator for a perfectly known system model subject to white, random disturbance processes (measurement and/or process noise) with known mean and covariance [13]. If the disturbance is Gaussian, then it is the optimal minimum covariance state estimator. When estimating the local bulk fluid flow in a wind field, the higher frequency fluctuations are not well-approximated as a Gaussian, white random disturbance process. Traditionally, this has been overcome by using a shaping filter such as the Dryden turbulence model which is driven by Gaussian, white noise. However, such probabilistic models for the atmospheric disturbance process are often poor approximations. Often, this information is either unknown or the turbulence models do not sufficiently capture the atmospheric dynamics. This is especially true at low altitudes and in urban environments where wind data are especially valuable for establishing boundary conditions used in numerical weather predictions [14]. To address this problem, we propose an H-infinity (H_∞) filtering approach to wind estimation, which makes *no assumptions* about the statistics of the disturbance, but instead assumes the system is subject to arbitrary finite-energy exogenous inputs. The optimal H_∞ filter does not aim to minimize estimate error in a quadratic sense, but rather minimizes the worst-case measure of the mapping from disturbances to estimate error. Limiting the worst-case error is a useful feature of a wind estimator for the applications mentioned. The H_∞ approach is thus an attractive alternative to the Kalman-Bucy filter, and similar alternatives, for the problem of estimating bulk wind flow in turbulent conditions.

In Section II, the aircraft motion model used to develop the state estimators is presented. Section III introduces the H_∞ filter. Section IV presents the steps involved in the synthesis of the H_∞ filter and introduces the Kalman-Bucy filter used for comparison. Section V presents the results of applying the two filters to experimental flight test data. Section VI presents conclusions.

II. Aircraft Motion in Wind

In developing the aircraft motion model for model-based estimation, we begin by defining the wind field. We then present a nonlinear flight dynamic model, with a common simplification (Assumption 1) for the effect of wind on the aircraft, and linearize about an arbitrary steady motion. Last, we incorporate a low-pass filter that allows the user to tune the frequency content of the wind estimates within the limits of the aircraft dynamic response, acknowledging that wind fluctuations are far more complex (Assumption 2) than the first simplifying assumption allows.

A. Wind Field

Consider an aircraft in a wind velocity field, $\boldsymbol{W}$, that varies in space and time. At an instant of time, the wind velocity that

This is the published version of the technical note available in the Journal of Guidance, Control, and Dynamics. DOI: 10.2514/1.G007735:

*Ph.D. Graduate, Kevin T. Crofton Department of Aerospace and Ocean Engineering; also Experimental Test Combat Systems Officer and Major, United States Air Force. Member AIAA.

†Ph.D. Candidate, Kevin T. Crofton Department of Aerospace and Ocean Engineering, Student Member AIAA

‡Professor, Kevin T. Crofton Department of Aerospace and Ocean Engineering, Associate Fellow AIAA

Copyright © 2024 by Jeremy W. Hopwood

would exist at the aircraft center of gravity (CG) if the aircraft were absent, the *apparent wind*, is

$$\boldsymbol{w}(t) = \boldsymbol{W}\left(\boldsymbol{X}(t), t\right) \tag{1}$$

where $\boldsymbol{X} = [X_N \;\; X_E \;\; X_D]^\mathsf{T}$ is the north-east-down position of the aircraft CG in a reference frame $\mathcal{F}_\mathrm{I}$. Although $\mathcal{F}_\mathrm{I}$ is fixed to the Earth's surface, we consider it to be an inertial reference frame, as is commonly done over short time intervals, and we define it using the orthonormal triad $\{\boldsymbol{i}_1, \boldsymbol{i}_2, \boldsymbol{i}_3\}$. The total time derivative of the apparent wind is

$$\frac{\mathrm{d}\boldsymbol{w}}{\mathrm{d}t} = \frac{\partial \boldsymbol{W}\left(\boldsymbol{X}, t\right)}{\partial t} + \frac{\partial \boldsymbol{W}\left(\boldsymbol{X}, t\right)}{\partial \boldsymbol{X}} \frac{\mathrm{d}\boldsymbol{X}}{\mathrm{d}t} \tag{2}$$

Adopting the standard overdot notation, $\dot{(\,)}$, for the total time derivative, and suppressing the arguments, gives

$$\dot{\boldsymbol{w}} = \frac{\partial \boldsymbol{W}}{\partial t} + \frac{\partial \boldsymbol{W}}{\partial \boldsymbol{X}} \dot{\boldsymbol{X}} \tag{3}$$

B. Aircraft Nonlinear Equations of Motion in Wind

Having introduced the dynamics of the wind field in Section II.A we now briefly present the aircraft equations of motion relative to the wind. The reader is directed to [15] and [16] for a full treatment of the derivation. Begin by defining the orthonormal aircraft body reference frame, $\mathcal{F}_\mathrm{B}$, defined by unit vectors $\{\boldsymbol{b}_1, \boldsymbol{b}_2, \boldsymbol{b}_3\}$ originating at the CG, where $\boldsymbol{b}_1$ points forward, $\boldsymbol{b}_2$ points out the right wing, and $\boldsymbol{b}_3$ completes the right-handed reference frame. The transformation mapping free vectors from $\mathcal{F}_\mathrm{B}$ to $\mathcal{F}_\mathrm{I}$ is given by the rotation matrix

$$\boldsymbol{R}_\mathrm{IB}(\boldsymbol{\Theta}) = e^{[\boldsymbol{e}_3\times]\psi} e^{[\boldsymbol{e}_2\times]\theta} e^{[\boldsymbol{e}_1\times]\phi} \tag{4}$$

where $\boldsymbol{\Theta} = [\phi \;\; \theta \;\; \psi]^\mathsf{T}$ is the vector comprising the aircraft roll, pitch, and yaw Euler angles, respectively. Here, $\boldsymbol{e}_1 = [1\;0\;0]^\mathsf{T}$, etc., and $[(\cdot)\times]$ is the skew-symmetric cross product equivalent matrix satisfying $[\boldsymbol{a}\times]\boldsymbol{b} = \boldsymbol{a}\times\boldsymbol{b}$. Note that $\boldsymbol{R}_\mathrm{BI}(\boldsymbol{\Theta}) := \boldsymbol{R}_\mathrm{IB}^{-1}(\boldsymbol{\Theta}) = \boldsymbol{R}_\mathrm{IB}^\mathsf{T}(\boldsymbol{\Theta})$ because $\boldsymbol{R}_\mathrm{IB}$ is orthonormal. The aircraft kinematics are given by

$$\dot{\boldsymbol{X}} = \boldsymbol{R}_\mathrm{IB}(\boldsymbol{\Theta})\boldsymbol{v} \tag{5}$$

$$\dot{\boldsymbol{R}}_\mathrm{IB}(\boldsymbol{\Theta}) = \boldsymbol{R}_\mathrm{IB}(\boldsymbol{\Theta})[\boldsymbol{\omega}\times] \tag{6}$$

where $\boldsymbol{v} = [u \;\; v \;\; w]^\mathsf{T}$ is the aircraft velocity with respect to the inertial frame and $\boldsymbol{\omega} = [p \;\; q \;\; r]^\mathsf{T}$ is the aircraft angular velocity with respect to the inertial frame, where both $\boldsymbol{v}$ and $\boldsymbol{\omega}$ are expressed in the body frame. While the matrix differential Eq. (6) holds for any parameterization of $\boldsymbol{R}_\mathrm{IB}$, adopting Euler angles gives the more compact system

$$\dot{\boldsymbol{\Theta}} = \boldsymbol{L}_\mathrm{IB}(\boldsymbol{\Theta})\boldsymbol{\omega} = \begin{bmatrix} 1 & \sin\phi\tan\theta & \cos\phi\tan\theta \\ 0 & \cos\phi & -\sin\phi \\ 0 & \sin\phi\sec\theta & \cos\phi\sec\theta \end{bmatrix} \begin{bmatrix} p \\ q \\ r \end{bmatrix} \tag{7}$$

Recall that the aerodynamic forces, $\boldsymbol{F}$, and moments, $\boldsymbol{M}$, depend on the velocity of the aircraft relative to the wind. Let

$$\boldsymbol{v}_\mathrm{r} = \boldsymbol{v} - \boldsymbol{R}_\mathrm{BI}(\boldsymbol{\Theta})\boldsymbol{w} \tag{8}$$

where $\boldsymbol{v}_\mathrm{r} = [u_\mathrm{r} \;\; v_\mathrm{r} \;\; w_\mathrm{r}]^\mathsf{T}$ is the velocity of the body's center of mass with respect to the wind, given in the body frame. Eq. (8) is known as the wind triangle. To simplify the derivation of the aircraft equations of motion, the following assumption is adopted:

Assumption 1 *The air-relative translational and angular accelerations due temporal and spatial variation in the wind field are negligible. In other words, $\frac{\partial \boldsymbol{W}}{\partial t}$ and $\frac{\partial \boldsymbol{W}}{\partial \boldsymbol{X}}$ are ignored in the aircraft dynamics.*

Assumption 1 may seem incompatible with the motivating challenge of estimating variations in the wind velocity. However, the assumption does not impede the model-based filter from adjusting wind velocity estimates based on measurements. This assumption, which is consistent with [2, 17], could be relaxed but it simplifies the results presented here for the H_∞ filter. One consequence of Assumption 1 is that the air relative angular velocity is equal to the vehicle angular velocity, $\boldsymbol{\omega}$. We therefore assume that the aerodynamic forces and moments have the general dependence

$$\boldsymbol{F} = \boldsymbol{F}(\boldsymbol{v}_\mathrm{r}, \boldsymbol{\omega}, \boldsymbol{u}), \quad \boldsymbol{M} = \boldsymbol{M}(\boldsymbol{v}_\mathrm{r}, \boldsymbol{\omega}, \boldsymbol{u}) \tag{9}$$

where $\boldsymbol{u} = [\delta_T \;\; \delta_a \;\; \delta_e \;\; \delta_r]^\mathsf{T}$ are the throttle, aileron, elevator, and rudder control inputs, respectively.

The aerodynamic model was found using the methods from [18] and references therein. The model has non-dimensional coefficients of the form

$$C_X = C_{X_o} + C_{X_\alpha}\alpha + C_{X_{\alpha^2}}\alpha^2 + C_{X_{\delta_\mathrm{e}}}\delta_\mathrm{e} + C_T\delta_T \tag{10a}$$

$$C_Z = C_{Z_o} + C_{Z_\alpha}\alpha + C_{Z_q}\hat{q} \tag{10b}$$

$$C_m = C_{m_o} + C_{m_\alpha}\alpha + C_{m_q}\hat{q} + C_{m_{\delta_\mathrm{e}}}\delta_\mathrm{e} \tag{10c}$$

$$C_Y = C_{Y_\beta}\beta + C_{Y_p}\hat{p} + C_{Y_r}\hat{r} + C_{Y_{\delta_\mathrm{a}}}\delta_\mathrm{a} + C_{Y_{\delta_\mathrm{r}}}\delta_\mathrm{r} \tag{10d}$$

$$C_l = C_{l_\beta}\beta + C_{l_p}\hat{p} + C_{l_{\delta_\mathrm{a}}}\delta_\mathrm{a} \tag{10e}$$

$$C_n = C_{n_\beta}\beta + C_{n_r}\hat{r} + C_{n_{\delta_\mathrm{a}}}\delta_\mathrm{a} + C_{n_{\delta_\mathrm{r}}}\delta_\mathrm{r} \tag{10f}$$

where the propulsion coefficient, C_T, is modeled using information from [19]. Here, an overhat $(\hat{\,})$ indicates a nondimensional angular rate. (The same notation will later be used to denote an estimate of a state variable.) The angle-of-attack, α, and angle-of-sideslip, β, are defined as follows:

$$\alpha = \tan^{-1}\left(\frac{w_\mathrm{r}}{u_\mathrm{r}}\right) \qquad \text{and} \qquad \beta = \sin^{-1}\left(\frac{v_\mathrm{r}}{V_\mathrm{r}}\right) \tag{11}$$

where $V_\mathrm{r} = \|\boldsymbol{v}_\mathrm{r}\|$. Note that Eqs. (9) and (10) omit the common quasi-steady approximations of unsteady effects (e.g., $\dot{\alpha}$ and $\dot{\beta}$). Thus, the well established nonlinear equations of motion, covered at length in [15, 20], adapted for the assumed wind field are

$$\dot{\boldsymbol{X}} = \boldsymbol{R}_\mathrm{IB}(\boldsymbol{\Theta})\boldsymbol{v}_\mathrm{r} + \boldsymbol{w} \tag{12a}$$

$$\dot{\boldsymbol{\Theta}} = \boldsymbol{L}_\mathrm{IB}(\boldsymbol{\Theta})\boldsymbol{\omega} \tag{12b}$$

$$\dot{\boldsymbol{v}}_\mathrm{r} = \boldsymbol{v}_\mathrm{r}\times\boldsymbol{\omega} + g\boldsymbol{R}_\mathrm{BI}(\boldsymbol{\Theta})\boldsymbol{e}_3 + \frac{1}{m}\boldsymbol{F}(\boldsymbol{v}_\mathrm{r}, \boldsymbol{\omega}, \boldsymbol{u}) \tag{12c}$$

$$\dot{\boldsymbol{\omega}} = \boldsymbol{I}^{-1}\left(\boldsymbol{I}\boldsymbol{\omega}\times\boldsymbol{\omega} + \boldsymbol{M}(\boldsymbol{v}_\mathrm{r}, \boldsymbol{\omega}, \boldsymbol{u})\right) \tag{12d}$$

where $\boldsymbol{I}$ is the matrix of aircraft moments and products of inertia as computed in $\mathcal{F}_B$. At last, the aircraft state and measurement equations are

$$\dot{\boldsymbol{x}} = \boldsymbol{f}(\boldsymbol{x}, \boldsymbol{u}, \boldsymbol{w}) \tag{13a}$$

$$\boldsymbol{y} = \boldsymbol{h}(\boldsymbol{x}, \boldsymbol{u}, \boldsymbol{\nu}) \tag{13b}$$

where the state, input, and wind vectors are

$$\boldsymbol{x} = \begin{bmatrix} \boldsymbol{X}^\mathsf{T} & \boldsymbol{\Theta}^\mathsf{T} & \boldsymbol{v}_\mathrm{r}^\mathsf{T} & \boldsymbol{\omega}^\mathsf{T} \end{bmatrix}^\mathsf{T}, \ \boldsymbol{u} = \begin{bmatrix} \delta_T & \delta_a & \delta_e & \delta_r \end{bmatrix}^\mathsf{T}, \quad \boldsymbol{w} = \begin{bmatrix} w_N & w_E & w_D \end{bmatrix}^\mathsf{T} \tag{14}$$

and where $\boldsymbol{\nu}$ is an unknown finite-energy measurement disturbance (i.e., noise), which is described further in Section III. We will now present the linearized equations of motion for the aircraft in a wind field.

C. Aircraft Linear Equations of Motion

For the purpose of estimating the wind, it is assumed that the aircraft state of motion remains in the neighborhood of a nominal, equilibrium flight condition over a desired time or distance. The most general steady motion for a fixed-wing aircraft is a steady turn at constant climb rate [15, §5.9]. This nominal flight condition is defined with regard to the *mean* wind field which, again, is assumed to be steady and uniform for the purpose of the flight dynamic model. Let $\boldsymbol{x}_\mathrm{eq}$, $\boldsymbol{u}_\mathrm{eq}$, and $\boldsymbol{w}_\mathrm{eq} = \boldsymbol{0}$ denote the state and control variables and the mean wind velocity corresponding to a given, steady flight condition such as a coordinated turn in still air. (Although we allow for accelerated steady motions, such as turning flight, we will use the term "equilibrium" and the subscript "eq" when referring to the nominal flight condition.) Having defined a nominal, equilibrium state of motion, and assuming that the flight dynamic model is exact, any perturbations from the equilibrium flight condition that are not attributed to the initial state or control inputs can be ascribed to the wind disturbance.

To prepare for the formulation of the H_∞ filter given in Section III, it is necessary to develop a linear time-invariant (LTI) model from the equations of motion given in Section II.B. Define

$$\boldsymbol{A} = \left.\frac{\partial \boldsymbol{f}}{\partial \boldsymbol{x}}\right|_{\boldsymbol{x}_\mathrm{eq}, \boldsymbol{u}_\mathrm{eq}, \boldsymbol{w}_\mathrm{eq}} \quad \boldsymbol{B} = \left.\frac{\partial \boldsymbol{f}}{\partial \boldsymbol{u}}\right|_{\boldsymbol{x}_\mathrm{eq}, \boldsymbol{u}_\mathrm{eq}, \boldsymbol{w}_\mathrm{eq}} \quad \boldsymbol{\Pi} = \left.\frac{\partial \boldsymbol{f}}{\partial \boldsymbol{w}}\right|_{\boldsymbol{x}_\mathrm{eq}, \boldsymbol{u}_\mathrm{eq}, \boldsymbol{w}_\mathrm{eq}} \tag{15}$$

The linear perturbation equations are

$$\Delta\dot{\boldsymbol{x}}(t) = \boldsymbol{A}\Delta\boldsymbol{x}(t) + \boldsymbol{B}\Delta\boldsymbol{u}(t) + \boldsymbol{\Pi}\Delta\boldsymbol{w}(t), \ \Delta\boldsymbol{x}(0) = \Delta\boldsymbol{x}_\mathbf{0} \tag{16a}$$

$$\Delta\boldsymbol{y}(t) = \boldsymbol{C}\Delta\boldsymbol{x}(t) + \boldsymbol{D}\Delta\boldsymbol{u}(t) + \boldsymbol{\Lambda}\boldsymbol{\nu} \tag{16b}$$

where $\Delta\boldsymbol{x}$, $\Delta\boldsymbol{u}$, and $\Delta\boldsymbol{w}$ are perturbations from the equilibrium state, control, and wind vectors. Additionally, $\Delta\boldsymbol{y}$ is the measurement perturbation, $\boldsymbol{C}$ and $\boldsymbol{D}$ are the output and feedthrough matrices, respectively, and $\boldsymbol{\Lambda}$ is the measurement noise input matrix. For brevity, we will drop the Δ and (t) notation.

D. Augmented Low-pass Filter

As was motivated in Section I, we often wish to estimate the mean wind in the presence of disturbances. Thus, we present the following assumption:

Assumption 2 *The wind is a superposition of a bulk flow velocity (constant or slowly varying), $\overline{\boldsymbol{w}}$, and a higher frequency, finite-energy disturbance (gusts or turbulence), $\delta\boldsymbol{w}$, so that*

$$\boldsymbol{w}(t) = \overline{\boldsymbol{w}}(t) + \delta\boldsymbol{w}(t) \tag{17}$$

Eq. (17) is known as a Reynolds decomposition [21] of the wind.

With Assumption 2 in place, we can design a low-pass filter $\boldsymbol{H}_{\overline{\boldsymbol{w}}}(s)$ to isolate the wind fluctuations of interest such that

$$\overline{\boldsymbol{w}}(s) = \boldsymbol{H}_{\overline{\boldsymbol{w}}}(s)\boldsymbol{w}(s) \tag{18}$$

where $\boldsymbol{w}(s)$ is the Laplace transform of $\boldsymbol{w}(t)$. Suppose Eq. (18) has the *state-space* realization

$$\dot{\boldsymbol{\zeta}} = \boldsymbol{A}_{\overline{\boldsymbol{w}}}\boldsymbol{\zeta} + \boldsymbol{B}_{\overline{\boldsymbol{w}}}\boldsymbol{w} \tag{19a}$$

$$= \boldsymbol{A}_{\overline{\boldsymbol{w}}}\boldsymbol{\zeta} + \boldsymbol{B}_{\overline{\boldsymbol{w}}}(\overline{\boldsymbol{w}} + \delta\boldsymbol{w}) \tag{19b}$$

$$\overline{\boldsymbol{w}} = \boldsymbol{C}_{\overline{\boldsymbol{w}}}\boldsymbol{\zeta} \tag{19c}$$

where $\boldsymbol{\zeta}$ is an intermediate state vector in the map from the wind input $\boldsymbol{w}$ to the output of interest, $\overline{\boldsymbol{w}}$. Combining this filter with the system in Eq. (16) gives the augmented system

$$\dot{\boldsymbol{x}}_A = \underbrace{\begin{bmatrix} \boldsymbol{A} & \boldsymbol{\Pi}\boldsymbol{C}_{\overline{\boldsymbol{w}}} \\ \boldsymbol{0} & \boldsymbol{A}_{\overline{\boldsymbol{w}}} + \boldsymbol{B}_{\overline{\boldsymbol{w}}}\boldsymbol{C}_{\overline{\boldsymbol{w}}} \end{bmatrix}}_{\boldsymbol{A}_A} \boldsymbol{x}_A + \underbrace{\begin{bmatrix} \boldsymbol{B} \\ \boldsymbol{0} \end{bmatrix}}_{\boldsymbol{B}_A} \boldsymbol{u} + \underbrace{\begin{bmatrix} \boldsymbol{\Pi} \\ \boldsymbol{B}_{\overline{\boldsymbol{w}}} \end{bmatrix}}_{\boldsymbol{\Pi}_A} \delta\boldsymbol{w}, \quad \boldsymbol{x}_A(0) = \boldsymbol{x}_{A_0} \tag{20a}$$

$$\boldsymbol{y}_A = \underbrace{\begin{bmatrix} \boldsymbol{C} & \boldsymbol{0} \end{bmatrix}}_{\boldsymbol{C}_A} \boldsymbol{x}_A + \boldsymbol{D}\boldsymbol{u} + \boldsymbol{\Lambda}\boldsymbol{\nu} \tag{20b}$$

where the augmented state is $\boldsymbol{x}_A = \begin{bmatrix} \boldsymbol{x}^\mathsf{T} & \boldsymbol{\zeta}^\mathsf{T} \end{bmatrix}^\mathsf{T}$. As will be shown in Section IV.B, we can use $\boldsymbol{H}_{\overline{\boldsymbol{w}}}(s)$ to specify the wind frequency content of interest. With the low-pass filter-augmented system defined, we can now discuss the H_∞ filter.

III. Steady-State H_∞ Filter

For the system described in this work the measurements do not directly depend on the inputs and thus $\boldsymbol{D} = \boldsymbol{0}$. Grouping the exogenous inputs to Eq. (20) as $\boldsymbol{\eta} := \begin{bmatrix} \delta\boldsymbol{w}^\mathsf{T} & \boldsymbol{\nu}^\mathsf{T} \end{bmatrix}^\mathsf{T}$ gives

$$\dot{\boldsymbol{x}}_A = \boldsymbol{A}_A\boldsymbol{x}_A + \boldsymbol{B}_A\boldsymbol{u} + \underbrace{\begin{bmatrix} \boldsymbol{\Pi} & \boldsymbol{0} \\ \boldsymbol{B}_{\overline{\boldsymbol{w}}} & \boldsymbol{0} \end{bmatrix}}_{\boldsymbol{G}} \boldsymbol{\eta} \tag{21a}$$

$$\boldsymbol{y}_A = \boldsymbol{C}_A\boldsymbol{x}_A + \underbrace{\begin{bmatrix} \boldsymbol{0} & \boldsymbol{\Lambda} \end{bmatrix}}_{\boldsymbol{F}} \boldsymbol{\eta} \tag{21b}$$

$$\boldsymbol{z} = \underbrace{\begin{bmatrix} \boldsymbol{L}_{\boldsymbol{x}} & \boldsymbol{0} \\ \boldsymbol{0} & \boldsymbol{C}_{\overline{\boldsymbol{w}}} \end{bmatrix}}_{\boldsymbol{L}} \boldsymbol{x}_A \tag{21c}$$

where z represents the outputs of interest when designing a filter that minimizes the worst-case effect of the exogenous disturbances, as will be shown presently. A Luenberger filter for the system of Eq. (21) is of the form

$$\dot{\hat{\boldsymbol{x}}}_A = \boldsymbol{A}_A\hat{\boldsymbol{x}}_A + \boldsymbol{B}_A\boldsymbol{u} + \boldsymbol{K}\left(\boldsymbol{y}_A - \boldsymbol{C}_A\hat{\boldsymbol{x}}_A\right), \quad \hat{\boldsymbol{x}}_A(0) = \hat{\boldsymbol{x}}_{A_0} \tag{22a}$$

$$\hat{\boldsymbol{z}} = \boldsymbol{L}\hat{\boldsymbol{x}}_A \tag{22b}$$

where the overhat, $(\hat{})$, now denotes a state estimate, rather than a non-dimensional angular rate, and where $\boldsymbol{K}$ is a generic filter gain matrix to be determined. Now define $\tilde{\boldsymbol{x}}_A = \boldsymbol{x}_A - \hat{\boldsymbol{x}}_A$. Thus, the error dynamics of the filter are

$$\dot{\tilde{\boldsymbol{x}}}_A = (\boldsymbol{A}_A - \boldsymbol{K}\boldsymbol{C}_A)\tilde{\boldsymbol{x}}_A + (\boldsymbol{G} - \boldsymbol{K}\boldsymbol{F})\boldsymbol{\eta} \tag{23a}$$

$$\tilde{\boldsymbol{z}} = \boldsymbol{z} - \hat{\boldsymbol{z}} = \boldsymbol{L}\tilde{\boldsymbol{x}}_A \tag{23b}$$

Let $\boldsymbol{H}_{\tilde{z}\eta}(s)$ represent the transfer function from exogenous inputs, $\boldsymbol{\eta}$, to estimate error, $\tilde{z}$ for the system (23). Also, recall from linear systems theory [22] that the H_∞ norm of system $\boldsymbol{H}_{\tilde{z}\eta}(s)$ is given by

$$\|\boldsymbol{H}_{\tilde{z}\eta}(s)\|_\infty = \operatorname*{ess\,sup}_{\omega_u \in \mathbb{R}} \sigma_{\max}\left(\boldsymbol{H}_{\tilde{z}\eta}(j\omega_u)\right) \tag{24}$$

where $\sigma_{\max}$ denotes the largest singular value. Additionally, define $\mathcal{L}_2[0,\infty)$ as the space of square-integrable functions with bounded energy such that

$$\boldsymbol{\eta} \in \mathcal{L}_2[0,\infty) \qquad \Rightarrow \qquad \int_0^\infty \|\boldsymbol{\eta}(t)\|_2^2 \mathrm{d}t < \infty \tag{25}$$

From [23, §7.8], we apply the following lemma:

Lemma 1 *(Adapted from Lemma 7.1(c) in [23]) For all* $\boldsymbol{\eta} \in \mathcal{L}_2[0,\infty)$*, for a given* $\gamma > 0$ *there exists a linear causal filter such that* $\boldsymbol{H}_{\tilde{z}\eta}(s)$ *is asymptotically stable and* $\|\boldsymbol{H}_{\tilde{z}\eta}(s)\|_\infty < \gamma$ *if and only if the algebraic Riccati inequality (ARI)*

$$\boldsymbol{A}_A^\mathsf{T}\boldsymbol{X} + \boldsymbol{X}\boldsymbol{A} - \boldsymbol{Y}\boldsymbol{C}_A - \boldsymbol{C}_A^\mathsf{T}\boldsymbol{Y}^\mathsf{T} + \gamma^{-2}\boldsymbol{L}^\mathsf{T}\boldsymbol{L} + (\boldsymbol{X}\boldsymbol{G} - \boldsymbol{Y}\boldsymbol{F})(\boldsymbol{X}\boldsymbol{G} - \boldsymbol{Y}\boldsymbol{F})^\mathsf{T} \prec \boldsymbol{0} \tag{26}$$

has a solution $\boldsymbol{X} = \boldsymbol{X}^\mathsf{T} \succ \boldsymbol{0}$ *and* $\boldsymbol{Y} \in \mathbb{R}^{n\times m}$*, where* n *is the number of states and* m *is the number of measurements. Applying the Schur complement to Eq. (26) yields the linear matrix inequality*

$$\boldsymbol{\mathcal{Y}} = \begin{bmatrix} \boldsymbol{A}_A^\mathsf{T}\boldsymbol{X} + \boldsymbol{X}\boldsymbol{A}_A - \boldsymbol{Y}\boldsymbol{C}_A - \boldsymbol{C}_A^\mathsf{T}\boldsymbol{Y}^\mathsf{T} + \gamma^{-2}\boldsymbol{L}^\mathsf{T}\boldsymbol{L} & \boldsymbol{X}\boldsymbol{G} - \boldsymbol{Y}\boldsymbol{F} \\ \boldsymbol{G}^\mathsf{T}\boldsymbol{X}^\mathsf{T} - \boldsymbol{F}^\mathsf{T}\boldsymbol{Y}^\mathsf{T} & -\boldsymbol{I} \end{bmatrix} \prec \boldsymbol{0} \tag{27a}$$

$$\boldsymbol{X} \succ \boldsymbol{0} \tag{27b}$$

Finally, the H_∞ *filter gain,* $\boldsymbol{K}_\infty$*, is*

$$\boldsymbol{K}_\infty = \boldsymbol{X}^{-1}\boldsymbol{Y} \tag{28}$$

Lemma 1 is valid for arbitrary finite-energy disturbances. As described in [23, §7.1], this is in contrast to traditional minimum variance filters, e.g., the well-known Kalman-Bucy filter. The H_∞ filter accepts noise as a deterministic disturbance with no *a priori* knowledge of the disturbance process required (e.g., mean, covariance, normality, whiteness, etc.), save for the assumption of bounded energy. This makes the H_∞ filter well-suited for applications where the characteristics of the noise are unknown, such as in the present problem of wind estimation.

IV. Filter Synthesis for Wind Estimation

A. Research Aircraft

The research aircraft used in this effort is the My Twin Dream (MTD), shown in Fig. 1, manufactured by My Fly Dream. It is a radio-controlled foam aircraft with counter-rotating twin electric motors and APC 10-in. diameter, 6-in. pitch (10x6) propellers. The aircraft was instrumented with a Cubepilot CubeOrange flight computer running PX4 firmware. The sensors onboard the aircraft include triple-redundant accelerometers and gyroscopes, two magnetometers, a real-time kinematic (RTK) global positioning system (GPS) receiver, and a vaned air data unit (ADU) for validating wind estimates. The MTD was chosen for its simple construction, propeller location (to accommodate the air data boom), and endurance of approximately 25 minutes. The MTD's physical properties are listed in Table 1. The parameters for the aerodynamic force and moment coefficients in Eq. (10) are given in [24]. The propulsion coefficient comes from a model based on the wind tunnel data from [19]. The accelerometers, gyroscopes, magnetometers and GPS produce a navigation solution as part of the PX4 firmware, from which we use position ($\boldsymbol{X}$), attitude ($\boldsymbol{\Theta}$), and angular velocity ($\boldsymbol{\omega}$) as measurements, $\boldsymbol{y}$, at a rate of 100 Hz. The PX4-provided $\boldsymbol{X}$, $\boldsymbol{\Theta}$,

Table 1 My Twin Dream (MTD) properties.

Property	Symbol	Value	Units
Mass	m	3.311	kg
Mean aerodynamic chord	$\bar{c}$	0.254	m
Projected wing span	b	1.800	m
Wing reference area	S	0.457	m^2
Roll moment of inertia	I_{xx}	0.319	$\mathrm{kg\text{-}m}^2$
Pitch moment of inertia	I_{yy}	0.267	$\mathrm{kg\text{-}m}^2$
Yaw moment of inertia	I_{zz}	0.471	$\mathrm{kg\text{-}m}^2$
Product of inertia	I_{xz}	0.024	$\mathrm{kg\text{-}m}^2$
Product of inertia	I_{xy}, I_{yz}	≈ 0	$\mathrm{kg\text{-}m}^2$

Fig. 1 My Twin Dream (MTD) aircraft.

and $\boldsymbol{\omega}$ estimates also include time-varying covariances, $\boldsymbol{E}(t)$ [25]. For our purposes these state estimate error covariances were averaged over the duration of a representative steady-maneuver, yielding the constant measurement noise covariance

$$\overline{\boldsymbol{E}} = \text{diag}\big(0.026\ \text{m}^2, 0.026\ \text{m}^2, 0.151\ \text{m}^2, 0.004\ \text{rad}^2, \\ 0.004\ \text{rad}^2, 0.054\ \text{rad}^2, 0.004\frac{\text{rad}^2}{\text{s}^2}, 0.004\frac{\text{rad}^2}{\text{s}^2}, 0.054\frac{\text{rad}^2}{\text{s}^2}\big) \tag{29}$$

1. Air Data Unit

The wind estimates were compared to reconstructed wind data from a vaned ADU mounted out the nose of the aircraft as pictured in Figure 1. The ADU provides *in situ* relative air velocity measurements. This sensor was developed, manufactured, and calibrated by the Nonlinear Systems Laboratory at Virginia Tech. It consists of two 3D printed vanes attached to magnetic rotary encoders and a 3D printed Kiel probe connected to a MS5525DSO* pressure sensor. The pulse-width modulation (PWM) rotary encoders are read at a sample rate of 200 Hz by a microcontroller that communicates with the flight computer over the CAN bus via a custom PX4 driver. The pressure sensor is natively supported by PX4 and configured to log calibrated airspeed data at 10 Hz.

Let V, α, and β_f be the airspeed, angle-of-attack, and flank angle reported by the ADU, respectively. By using GPS velocity measurements $\boldsymbol{v}_\text{i}$ (accuracy ≈ 0.05 m/s), autopilot attitude estimates (with quaternion estimate standard deviations $\approx 10^{-3}$), and angular velocity measurements from the calibrated gyroscope (noise and bias removed), the wind velocity may be reconstructed as

$$\boldsymbol{w} = \boldsymbol{v}_\text{i} - \boldsymbol{R}_\text{IB}\left(\boldsymbol{v}_\text{ADU} - \boldsymbol{\omega} \times \boldsymbol{r}_\text{ADU}\right) \tag{30}$$

where $\boldsymbol{v}_\text{ADU} = \boldsymbol{R}_\text{BW}(\alpha, \beta)\boldsymbol{e}_1 V_\text{r}$. Here, $\boldsymbol{v}_\text{ADU}$ is the air-relative velocity at the geometric center of the ADU vanes, whose position in the body frame is denoted $\boldsymbol{r}_\text{ADU}$. The rotation matrix $\boldsymbol{R}_\text{BW}(\alpha, \beta) = e^{-[\boldsymbol{e}_2\times]\alpha}e^{[\boldsymbol{e}_3\times]\beta}$, which maps free vectors from the wind frame to the body frame, is parameterized by the measured angle-of-attack, α, and the sideslip angle, $\beta = \tan^{-1}(\tan(\beta_f)\cos(\alpha))$. The accuracy of the reconstructed wind data can be characterized by propagating the measurement uncertainty through Eq. (30). Due to the low error of the constituent measurements, the reconstructed wind is treated as a truth source for wind estimate validation. This air data unit was validated in the Virginia Tech Aerospace and Ocean Engineering department's open jet wind tunnel both for steady-state readings and dynamic response. The airspeed-dependent cutoff frequencies of the vanes were found to be greater than 16 Hz, well above the fastest rigid body modes, which determine an upper limit on the dynamic response of model-based wind estimators.

2. Cascaded Filter Structure

The cascaded filter structure that is implemented on the MTD UAS is depicted in Fig. 2. The PX4 state estimates $\boldsymbol{X}$, $\boldsymbol{\Theta}$, and $\boldsymbol{\omega}$ are treated as measurements for the wind estimator (H_∞ or Kalman-Bucy filter). The wind estimator incorporates the 6 degree of freedom (DoF) aircraft model and frequency filter model from Section III and produces estimates of the aircraft states and the low-pass filtered wind. For validation, the H_∞ and Kalman-Bucy wind estimates are compared to direct low-pass ($\boldsymbol{H}_{\overline{\boldsymbol{w}}}$) filtered ADU wind measurements, $\overline{\boldsymbol{w}}$. Note that the wind estimators do not have access to the ADU measurements.

*Manufactured by TE Connectivity

B. H_∞ Filter Synthesis

The first step in synthesizing the H_∞ filter is to linearize Eq. (12) in preparation for creating the augmented system Eq. (21). To begin the linearization process, the trim states and controls of Eq. (12) are found via Matlab using a publicly available local minimizing function, `fminsa`, which is based on [26]. The nominal flight condition chosen for the results presented here is straight-and-level flight at a constant airspeed, heading, and altitude with zero wind. Any steady motion could be chosen, however, since linearizing the flight dynamics about a steady motion yields an LTI model, as required by the filtering methods considered here.

The nominal state and control values are used in a linearization routine to find the matrices of Eq. (16). The routine numerically approximates the Jacobians in Eq. (15) by adaptively reducing the perturbation stepsize. The resultant matrices $\boldsymbol{A}_{\boldsymbol{A}}$ and $\boldsymbol{B}_{\boldsymbol{B}}$ are omitted for brevity. The matrix $\boldsymbol{\Pi}$ is found to be $\mathbb{I}^{3\times3}$, where $\mathbb{I}^{a\times a}$ is an $a \times a$ identity matrix. The matrix is $\boldsymbol{H}_{\overline{\boldsymbol{w}}}$ is dictated by the choice of filter from Eq. (18).

For the present work, a first-order low-pass filter is implemented such that

$$\boldsymbol{H}_{\overline{\boldsymbol{w}}}(s) = \begin{bmatrix} \frac{\omega_\text{c}}{s+\omega_\text{c}} & 0 & 0 \\ 0 & \frac{\omega_\text{c}}{s+\omega_\text{c}} & 0 \\ 0 & 0 & \frac{\omega_\text{c}}{s+\omega_\text{c}} \end{bmatrix} \tag{31}$$

where ω_c is the desired cutoff frequency in rad/s. Therefore, $\boldsymbol{G}$ is

$$\boldsymbol{G} = \begin{bmatrix} \mathbb{I}^{3\times3} & \boldsymbol{0}^{3\times9} \\ \boldsymbol{0}^{9\times3} & \boldsymbol{0}^{9\times9} \\ \boldsymbol{B}_{\overline{\boldsymbol{w}}} & \boldsymbol{0}^{3\times9} \end{bmatrix} \tag{32}$$

where $\boldsymbol{0}^{a\times b}$ is an $a \times b$ matrix of zeros. The $\boldsymbol{C}_{\boldsymbol{A}}$ and $\boldsymbol{D}$ matrices are

$$\boldsymbol{C}_A = \begin{bmatrix} \mathbb{I}^{3\times3} & \boldsymbol{0}^{3\times3} & \boldsymbol{0}^{3\times3} & \boldsymbol{0}^{3\times3} & \boldsymbol{0}^{3\times3} \\ \boldsymbol{0}^{3\times3} & \mathbb{I}^{3\times3} & \boldsymbol{0}^{3\times3} & \boldsymbol{0}^{3\times3} & \boldsymbol{0}^{3\times3} \\ \boldsymbol{0}^{3\times3} & \boldsymbol{0}^{3\times3} & \boldsymbol{0}^{3\times3} & \mathbb{I}^{3\times3} & \boldsymbol{0}^{3\times3} \end{bmatrix} \quad \boldsymbol{D} = \begin{bmatrix} \boldsymbol{0}^{9\times4} \end{bmatrix} \tag{33}$$

since, for the avionics system described in Section IV.A, we have access to $\boldsymbol{X}$, $\boldsymbol{\Theta}$, and $\boldsymbol{\omega}$. To simplify the comparison between the H_∞ filter and the Kalman-Bucy filter in Section IV.C, we choose $\boldsymbol{\Lambda} = \overline{\boldsymbol{E}}$. More generally, $\boldsymbol{\Lambda}$ can be chosen by the user to describe the relative magnitude of measurement disturbances if that information is known. With our choice, the matrix $\boldsymbol{F}$ is

$$\boldsymbol{F} = \begin{bmatrix} \boldsymbol{0}^{9\times3} & \overline{\boldsymbol{E}} \end{bmatrix} \tag{34}$$

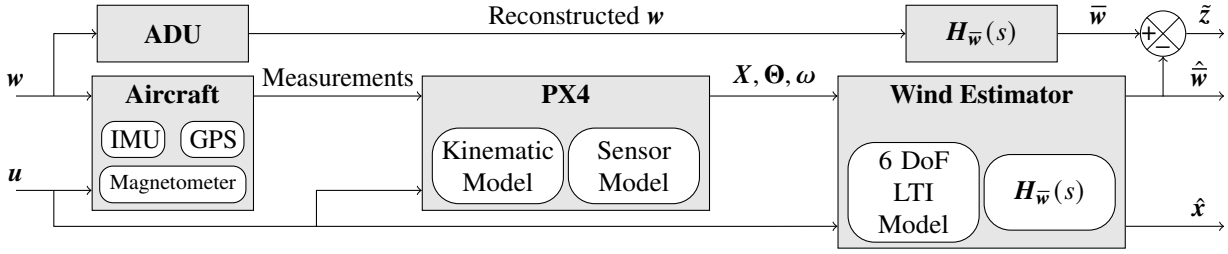

Fig. 2 Cascade filter architecture.

For this work, we only wish to place performance guarantees on the mean wind estimate, $z = \overline{w}$. Thus, the desired state estimate combination $\boldsymbol{L}$ from Eq. (21c) is

$$\boldsymbol{L} = \begin{bmatrix} \boldsymbol{0}^{3\times 12} & \boldsymbol{C}_{\overline{w}} \end{bmatrix} \tag{35}$$

Note that even though the other aircraft states are not included in the performance output, z, their estimate error remains bounded and is asymptotically stable for $\boldsymbol{\eta} = \boldsymbol{0}$. To obtain performance guarantees on the total state vector, the matrix $\boldsymbol{L}$ would be chosen accordingly. With all of the required matrices identified, Eq. (27) is solved using `CVX` in Matlab with the `SDPT3` solver [27–29] to find the optimal H_∞ filter gain by minimizing γ. For the example presented, here the worst-case disturbance amplification is $\gamma = 1.08$. Recalling Lemma 1, this means

$$\|\boldsymbol{H}_{\tilde{z}\eta}(s)\|_\infty = \sup_{\boldsymbol{\eta}\in\mathcal{L}_2} \frac{\|\tilde{\boldsymbol{z}}\|_2}{\|\boldsymbol{\eta}\|_2} < 1.08 \tag{36}$$

That is, the map from exogenous inputs to estimate error has a worst-case gain of 1.08.

C. Comparative Kalman-Bucy Filter

To provide a comparison to the H_∞ filter, a steady-state Kalman-Bucy filter was developed according to [23, §3.4.3] and [30, §8.1.2]. Using Eq. (20), the steady-state Kalman-Bucy filter is found by solving the continuous algebraic Riccati equation (ARE)

$$\boldsymbol{A}_A\boldsymbol{P} + \boldsymbol{P}\boldsymbol{A}_A^\mathsf{T} + \boldsymbol{Q} - \boldsymbol{P}\boldsymbol{C}_A^\mathsf{T}\boldsymbol{R}^{-1}\boldsymbol{C}_A\boldsymbol{P} = \boldsymbol{0} \tag{37}$$

where $\boldsymbol{P} = \boldsymbol{P}^\mathsf{T} > \boldsymbol{0}$. For the continuous-time Kalman-Bucy filter, $\boldsymbol{Q}$ and $\boldsymbol{R}$ are the process and measurement noise power spectral density matrices, satisfying

$$E[\delta\boldsymbol{w}(t)\delta\boldsymbol{w}^\mathsf{T}(\tau)] = \boldsymbol{Q}\delta(t-\tau) \tag{38}$$

$$E[\boldsymbol{\nu}(t)\boldsymbol{\nu}^\mathsf{T}(\tau)] = \boldsymbol{R}\delta(t-\tau) \tag{39}$$

These definitions are made under the assumption that $\delta\boldsymbol{w}$ and $\boldsymbol{\nu}$ are mutually uncorrelated, continuous-time, white noise. If $\delta\boldsymbol{w}$ and $\boldsymbol{\nu}$ are Gaussian, then the Kalman-Bucy filter provides the optimal estimate [23, §3.1]. Note that in general this is not the case for $\delta\boldsymbol{w}$, as turbulence is neither white nor Gaussian [31].

Following [30, §8.1.2], $\boldsymbol{R} = \overline{\boldsymbol{E}}T_s$ where the sample time $T_s = 0.01$ s, given the 100 Hz sample rate. The constant process noise power spectral density, $\boldsymbol{Q}$, was computed from a representative maneuver. Using truth data from the air data unit and the autopilot's state estimator, the difference between the true and modeled (Eq. 16) state derivative is computed. Then, $\boldsymbol{Q}$ is selected as the maximum power spectral density of this difference signal over all frequencies. Specifically, for the augmented wind states the $\boldsymbol{Q}$ matrix entries are the maximum power spectral density of $\delta\boldsymbol{w}$ (Eqs. (17) and (18)), calculated using the ADU measurements.

The ARE of Eq. (37) is solved for $\boldsymbol{P}$ using the Matlab function $\texttt{icare}(\boldsymbol{A}_A^\mathsf{T}, \boldsymbol{C}_A^\mathsf{T}, \boldsymbol{Q}, \boldsymbol{R})$. Finally, the Kalman-Bucy gain is found from

$$\boldsymbol{K}_\mathrm{K} = \boldsymbol{P}\boldsymbol{C}_A^\mathsf{T}\boldsymbol{R}^{-1} \tag{40}$$

The Kalman-Bucy filter is implemented in the same manner as the H_∞ filter using Eq. (22). Thus, the only difference between the Kalman-Bucy filter and the H_∞ filter presented in this work is the observer gain matrix $\boldsymbol{K}_\mathrm{K}$ versus $\boldsymbol{K}_\infty$. The gain matrices are obtained using distinctly different theoretical approaches, however, and as shown in the following section, the performance of these filters is significantly different.

V. Flight Test Results

A flight test campaign was conducted at Virginia Tech's Kentland Experimental Aerial Systems (KEAS) Laboratory airfield on September 28th, 2022 using the UAS described in Section IV.A. Data were gathered during four passes over the ground control station (referred to as runs 1-4) at 76 m (250 ft) AGL when the wind conditions at ground level were gusty. The test runs are shown in Fig. 3, where light orange segments are paths connecting user-specified waypoints, chosen to align with the cardinal directions, while the red curve shows the actual aircraft path. The wide blue arrows, numbered 1, 2, 3, and 4, are the four passes mentioned above. The prevailing wind was out of the northwest. Gusty conditions were chosen since the goal is to achieve accurate wind estimates under any condition in which the UAS is able to fly. Since we are utilizing an LTI model we restricted our maneuver to steady flight, specifically straight-and-level unaccelerated flight. To evaluate the performance of the filters three different cutoff frequencies $\omega_\mathrm{c} \in \{0.5, 2, 5\}$ rad/s were chosen for the low-pass filter (31) to capture slow, medium, and fast wind fluctuations, respectively [32].

Figs. 4-6 show the results of the H_∞ and Kalman-Bucy (K-B) filters, as applied to the system in Eq. (20), using Run 3 from flight test data. For validation, the wind estimates are compared to low-pass filtered ADU wind measurements. Run 3 was chosen because it exhibits the largest wind fluctuations in all three directions.

In Fig. 4, the low-pass filter cutoff frequency is 0.5 rad/s,

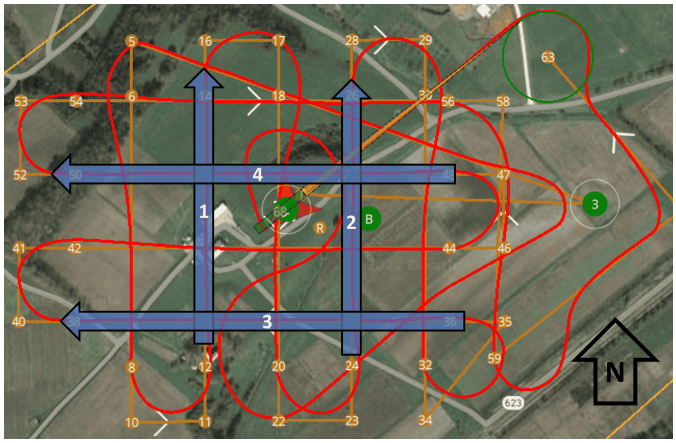

Fig. 3 Runs 1-4 from September 28th, 2022 flight test campaign. The prevailing wind was out of the northwest during the test campaign.

which corresponds to the relatively slow bulk flow of the wind. As can be seen the H_∞ filter more closely tracks the filtered wind shown in the dashed black line in the north and south direction compared to the Kalman-Bucy filter. Conversely, the Kalman-Bucy filter has marginally better accuracy in the down direction. Figs. 5 and 6 present the results using a cutoff frequency of 2 and 5 rad/s, respectively, and thus capture higher frequency fluctuations. In both cases the H_∞ filter outperforms the Kalman-Bucy filter.

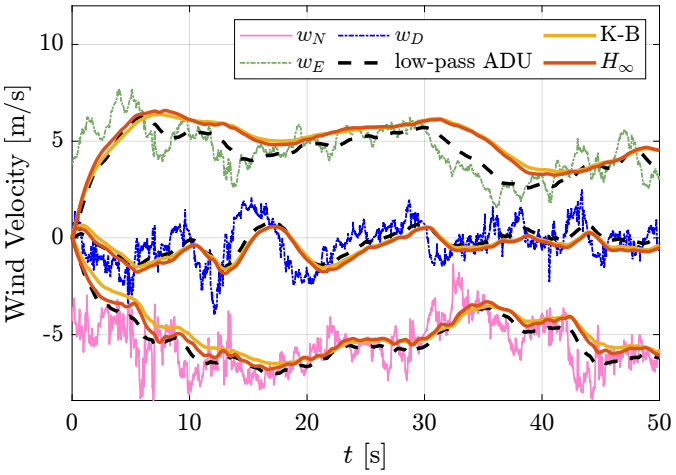

Fig. 4 Results from Run 3 with $\omega_c = 0.5$ rad/s.

Lastly, Table 2 presents the root-mean-square (RMS) error between the filter estimates and the low-pass filtered ADU measurements for all four runs. The H_∞ filter estimates are more accurate in all three directions, except for w_D with $\omega_c = 0.5$ rad/s as discussed above. In these cases, however, the Kalman-Bucy filter estimates are only marginally better. Conversely, in several of the cases tested the H_∞ filter estimates exhibit roughly half the error of the corresponding Kalman-Bucy filter estimate.

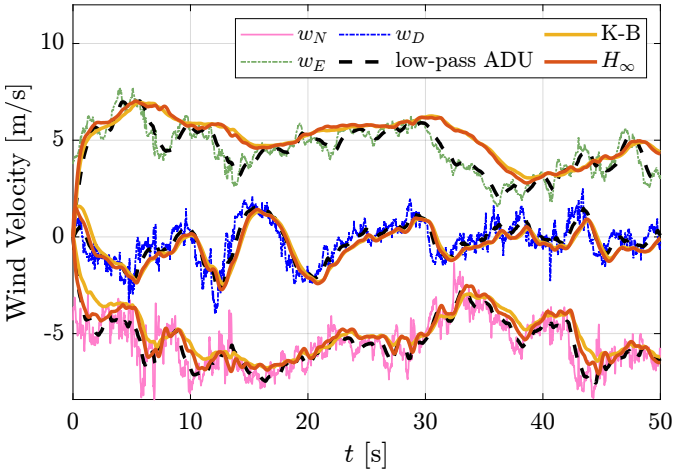

Fig. 5 Results from Run 3 with $\omega_c = 2$ rad/s.

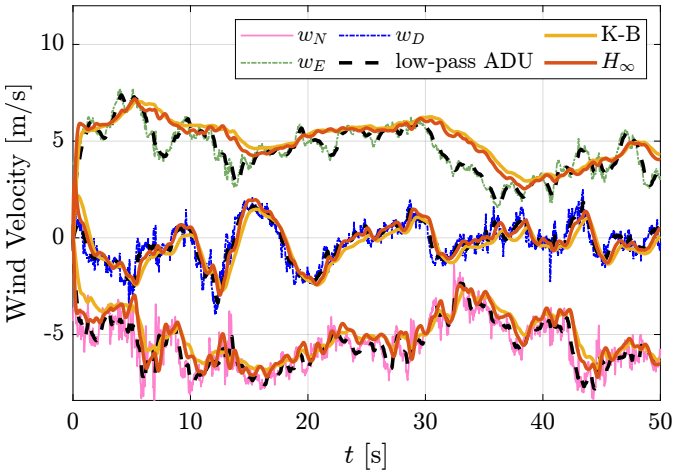

Fig. 6 Results from Run 3 with $\omega_c = 5$ rad/s.

VI. Conclusions

This paper describes the concatenation of a low-pass filter and a flight dynamic model which are then used to estimate the bulk wind velocity despite the presence of turbulence. Unlike a Kalman-Bucy filter, the H_∞ filter requires minimal assumptions about the process noise (i.e., turbulence) and measurement noise and is thus more applicable to wind estimation where the wind fluctuations cannot be assumed to be white, Gaussian noise. In contrast to the Kalman-Bucy filter, the proposed H_∞ filter provides a guarantee on the worst-case error in the form of a bounded mapping from the wind disturbance inputs to the wind estimate error. Even in cases where both filters perform similarly, the Kalman filter loses its theoretical benefits due to the violation of its assumptions, whereas the H_∞ filter retains its theoretical guarantees. Furthermore, the inclusion of a low-pass filter provides flexibility in specifying the upper frequency limit of the wind variations one wishes to estimate. The combined low-pass filter and H_∞ filter approach offers an effective means of obtaining accurate wind estimates within a desired frequency band while requiring minimal assumptions about the spectral character of the wind disturbances.

Table 2 Root-mean-square error between filter estimates and direct low-pass filter of measured wind. Error results in bold are the lesser of the two filters. Note K-B = Kalman-Bucy.

Filter	Wind Direction	Cutoff Freq. (ω_c) [rad/s]	Flight Test Run (error in [m/s]) 1	2	3	4	Average Error [m/s]
H_∞	w_N	0.5	**0.496**	**0.576**	**0.402**	**0.367**	**0.460**
		2	**0.664**	**0.713**	**0.493**	**0.451**	**0.580**
		5	**0.703**	**0.663**	**0.635**	**0.544**	**0.636**
	w_E	0.5	**0.521**	**0.657**	**0.776**	**0.669**	**0.655**
		2	**0.624**	**0.685**	**0.905**	**0.698**	**0.728**
		5	**0.611**	**0.710**	**0.854**	**0.608**	**0.696**
	w_D	0.5	0.213	0.236	0.347	0.385	0.295
		2	**0.237**	**0.210**	**0.355**	**0.333**	**0.284**
		5	**0.281**	**0.313**	**0.321**	**0.290**	**0.301**
K-B	w_N	0.5	0.665	1.089	0.557	0.510	0.705
		2	0.796	1.201	0.610	0.614	0.805
		5	0.874	1.236	0.690	0.685	0.871
	w_E	0.5	0.666	0.854	0.825	0.899	0.811
		2	0.798	0.937	0.938	0.924	0.899
		5	0.867	0.963	0.992	0.945	0.942
	w_D	0.5	**0.191**	**0.225**	**0.254**	**0.382**	**0.263**
		2	0.318	0.320	0.403	0.492	0.383
		5	0.440	0.423	0.534	0.610	0.502
Flight Direction			North	North	West	West	

Acknowledgements

The authors gratefully acknowledge the sponsorship of NASA under Grant No. 80NSSC20M0162, as well as the support of the U.S. Air Force and Virginia Tech's Kevin T. Crofton Department of Aerospace and Ocean Engineering. The authors would also like to thank Dr. Mekonen H. Halefom for his support during flight-test activities.

References

[1] Jacob, J. D., Chilson, P. B., Houston, A. L., and Smith, S. W., "Considerations for Atmospheric Measurements with Small Unmanned Aircraft Systems," *Atmosphere*, Vol. 9, No. 7, 2018, p. 252. https://doi.org/10.3390/atmos9070252.

[2] González-Rocha, J., De Wekker, S. F. J., Ross, S. D., and Woolsey, C. A., "Wind Profiling in the Lower Atmosphere from Wind-Induced Perturbations to Multirotor UAS," *Sensors*, Vol. 20, No. 5:1341, 2020. https://doi.org/10.3390/s20051341.

[3] Fuhrmann, M., and Horowitz, M. C., "Droning on: Explaining the Proliferation of Unmanned Aerial Vehicles," *International Organization*, Vol. 71, No. 2, 2017, pp. 397–418. https://doi.org/10.1017/S0020818317000121.

[4] Wang, T., Zhong, W., Qian, Y., and Zhu, C., *Reynolds-Averaged Navier–Stokes Method for Wind Turbine Simulations*, Springer Nature Singapore, Singapore, 2023, Chap. 11, pp. 193–211. https://doi.org/10.1007/978-981-99-3509-3_11.

[5] Chrit, M., "Reconstructing urban wind flows for urban air mobility using reduced-order data assimilation," *Theoretical and Applied Mechanics Letters*, Vol. 13, No. 4, 2023. https://doi.org/10.1016/j.taml.2023.100451.

[6] Lie, F., and Gebre-Egziabher, D., "Synthetic Air Data System," *Journal of Aircraft*, Vol. 50, 2013, pp. 1234–1249. https://doi.org/10.2514/1.C032177.

[7] Lee, J. H., Sevil, H., Dogan, A., and Hullender, D., "Estimation of Maneuvering Aircraft States and Time-Varying Wind with Turbulence," *AIAA Guidance, Navigation, and Control Conference*, Minneapolis, MN, 2012, pp. 1–23. https://doi.org/10.2514/6.2012-4532.

[8] Ahmed, Z., Halefom, M. H., and Woolsey, C. A., "A Survey of Wind Estimation Methods using Small Uncrewed Aerial Vehicles," *Journal of Aerospace Information Systems (Accepted, In Review)*, 2024.

[9] Tian, P., Chao, H., Rhudy, M., Gross, J., and Wu, H., "Wind Sensing and Estimation Using Small Fixed-Wing Unmanned Aerial Vehicles: A Survey," *Journal of Aerospace Information Systems*, Vol. 18, No. 3, 2021, pp. 132–143. https://doi.org/10.2514/1.I010885.

[10] Hajiyev, C., Cilden-Guler, D., and Hacizade, U., "Two-Stage Kalman Filter for Estimation of Wind Speed and UAV Flight Parameters based on GPS/INS and Pitot Tube Measurements," *2019 9th International Conference on Recent Advances in Space Technologies (RAST)*, Institute of Electrical and Electronics Engineers, Istanbul, Turkey, 2019, pp. 875–880. https://doi.org/10.1109/RAST.2019.8767886.

[11] Sun, S., Dong, K., Guo, C., and Tan, D., "A Wind Estimation Based on Unscented Kalman Filter for Standoff Target Tracking Using a Fixed-Wing UAV," *International Journal of Aeronautical and Space Sciences*, Vol. 22, No. 2, 2021, pp. 366–375. https://doi.org/10.1007/s42405-020-00290-7.

[12] Langelaan, J. W., Spletzer, J., Montella, C., and Grenestedt, J., "Wind Field Estimation for Autonomous Dynamic Soaring," *2012 IEEE International Conference on Robotics and Automation*, 2012, pp. 16–22. https://doi.org/10.1109/ICRA.2012.6224954.

[13] Bar-Shalom, Y., Li, X., and Kirubarajan, T., *Estimation with Applications to Tracking and Navigation: Theory Algorithms and Software*, John Wiley & Sons, New York, 2004, Chap. 5, pp. 200–215. https://doi.org/10.1002/0471221279.

[14] National Research Council, *Observing Weather and Climate from the Ground Up: Nationwide Network of Networks*, The National Academies Press, Washington, DC, 2009. https://doi.org/10.17226/12540.

[15] Etkin, B., *Dynamics of Atmospheric Flight*, John Wiley and Sons, New York, 1972, Chap. 5, pp. 121–157. https://doi.org/10.1017/S0001924000040380.

[16] Frost, W., and Bowles, R. L., "Wind Shear Terms in the Equations of Aircraft Motion," *Journal of Aircraft*, Vol. 21, No. 11, 1984, pp. 866–872. https://doi.org/10.2514/3.45056.

[17] González-Rocha, J., Woolsey, C. A., Sultan, C., and De Wekker, S. F. J., "Sensing Wind from Quadrotor Motion," *Journal of Guidance, Control, and Dynamics*, Vol. 42, No. 4, 2019, pp. 836–852. https://doi.org/10.2514/1.G003542.

[18] Simmons, B. M., Gresham, J. L., and Woolsey, C. A., "Flight-Test System Identification Techniques and Applications for Small, Low-Cost, Fixed-Wing Aircraft," *Journal of Aircraft*, Vol. 60, No. 5, 2023, pp. 1503–1521. https://doi.org/10.2514/1.C037260.

[19] Brandt, J., Deters, R., Ananda, G., Dantsker, O., and Selig, M., "UIUC Propeller Database,Vols 1-4," , Nov 2022. Retrieved from https://m-selig.ae.illinois.edu/props/propDB.html.

[20] Yechout, T. R., *Introduction to Aircraft Flight Mechanics*, 2nd ed., AIAA Education Series, American Institute of Aeronautics & Astronautics, Reston, VA, 2014, Chap. 4, pp. 163–192. https://doi.org/10.2514/4.102547.

[21] Kundu, P. K., and Cohen, I. M., *Fluid Mechanics*, 3rd ed., Elsevier Academic Press, San Diego, CA, 2004, Chap. 13, pp. 529–530. https://doi.org/10.1016/C2012-0-00611-4.

[22] Dullerud, G. E., and Paganini, F., *A Course in Robust Control Theory: A Convex Approach*, Springer-Verlag, New York, 2000, Chap. 3, pp. 101–135. https://doi.org/10.1007/978-1-4757-3290-0.

[23] Lewis, F., Xie, L., and Popa, D., *Optimal and Robust Estimation with an Introduction to Stochastic Control Theory*, 2nd ed., Taylor & Francis Group, LLC., Boca Raton, FL, 2008. https://doi.org/10.1201/9781315221656.

[24] Gahan, K. C., Hopwood, J. W., and Woolsey, C. A., "Uncertainty in Wind Estimates, Part 1: Analysis using Generalized Polynomial Chaos," *AIAA SCITECH Forum*, Orlanda, FL, 2024, pp. 1–15. https://doi.org/10.2514/6.2024-2824.

[25] Riseborough, P., "Using the ECL EKF," , Accessed Nov 2022. Retrieved from https://docs.px4.io/main/en/advanced_config.html.

[26] Dennis, J. E., and Woods, D. J., "Optimization on microcomputers: the Nelder–Mead simplex algorithm," *New Computing Environments: Microcomputers in Large-Scale Computing*, edited by A. Wouk, Society for Industrial and Applied Mathematics, Philadelphia, PA, 1987, pp. 116–122. https://doi.org/10.21236/ada453814.

[27] Toh, K. C., Todd, M. J., and Tütüncü, R. H., "SDPT3 — A Matlab software package for semidefinite programming, Version 1.3," *Optimization Methods and Software*, Vol. 11, No. 1-4, 1999, pp. 545–581. https://doi.org/10.1080/10556789908805762.

[28] Grant, M., and Boyd, S., "CVX: Matlab Software for Disciplined Convex Programming, V 2.1, Mar 2014," , Accessed May 2022. Retrieved from http://cvxr.com/cvx.

[29] Grant, M., and Boyd, S., "Graph implementations for nonsmooth convex programs," *Recent Advances in Learning and Control*, edited by V. Blondel, S. Boyd, and H. Kimura, Lecture Notes in Control and Information Sciences, Springer-Verlag Limited, 2008, pp. 95–110. http://stanford.edu/~boyd/graph_dcp.html.

[30] Simon, D., *Optimal State Estimation: Kalman, H_∞, and Nonlinear Approaches*, John Wiley & Sons, Inc., Hoboken, New Jersey, 2006. https://doi.org/10.1002/0470045345.

[31] Stull, R., *An Introduction to Boundary Layer Meteorology*, Kluwer Academic Publishers, Dordrecht, The Netherlands, 1988, Chap. 1, pp. 5–6. https://doi.org/10.1007/978-94-009-3027-8.

[32] Williams, J. K., and Meymaris, G., "Remote Turbulence Detection Using Ground-Based Doppler Weather Radar," *Aviation Turbulence: Processes, Detection, Predictions*, edited by R. Sharman and T. Lane, Springer International Publishing AG, Switzerland, 2016, pp. 149–177. https://doi.org/10.1007/978-3-319-23630-8.